

Research Article

Lateral Superharmonic Resonance of the Rotor in 12/8 Poles Switched Reluctance Motor

Feng Wang ^{1,2}, Zhiqiang Wu ^{1,2}, Yuancen Wang ^{1,2} and Yajie Li ^{1,2}

¹Department of Mechanics, School of Mechanical Engineering, Tianjin University, Tianjin 300072, China

²Tianjin Key Laboratory of Nonlinear Dynamics and Chaos Control, Tianjin University, Tianjin 300072, China

Correspondence should be addressed to Zhiqiang Wu; zhiqwu@tju.edu.cn

Received 10 May 2018; Accepted 16 August 2018; Published 10 September 2018

Academic Editor: Petr Krysl

Copyright © 2018 Feng Wang et al. This is an open access article distributed under the Creative Commons Attribution License, which permits unrestricted use, distribution, and reproduction in any medium, provided the original work is properly cited.

Switched reluctance motor (SRM) generates a very large electromagnetic radial force when the stator windings commutate because of its doubly salient structure and magnetic saturation. Lateral vibration appears when electromagnetic radial force is applied onto the rotational rotor, which causes continual changes of airgap and further radical electromagnetic force. Nonlinear vibration of the rotor under the interaction of electromagnetic radial force and displacement becomes very complicated, which is becoming a research hotspot at present. A whole lateral vibration dynamics equation is established by finite element method. The radical force formula of single rotor tooth was deduced by integration of equivalent electromagnetic circuit and Maxwell stress method, and final functional expression of radial electromagnetic resultant when stator windings are energized with ideal square wave is also obtained. The critical speeds and vibration modes of the rotor are analyzed by Campbell diagram and lateral vibration displacement locus is solved by Newmark-Beta numerical integration method. The results show that the vibration locus of the rotor distributes in a circular domain. The frequency distribution of electromagnetic resultant relates to rotation speed, current switch frequency, and current wave, while the frequency distribution of the displacement also closely relates to the first-order critical speed of the rotor. When the rotor runs at some specific speed, lateral superharmonic resonance phenomenon appears and its displacement locus shows rich diversity. Lateral vibration characteristic of the rotor could be quickly grasped through this study, which makes vibration evaluation possible for advanced motor design.

1. Introduction

Switched reluctance motors (SRM) are drawing great attention for variable speed motor drives due to its own advantages, such as simple structure, reliable power converter, good speed regulation performance, and good fault-tolerant capacity. They are suitable for applications such as electric vehicles, aircraft starter/generators systems, and mining drives [1]. However, great acoustic noise induced by the doubly salient structure and switch form power supply of the SRM has brought great challenges to the widespread development of SRM, especially in noise sensitive applications [2].

Radial vibration of the SRM stator core has been extensively studied so far through a variety of ways such as coupling simulation of multiple physical fields or radial force mutation to induce vibration at turn-off instant [3–7]. However, because of the great difficulty in the characterization of electromagnetic radical force when the SRM

is running, the research about the lateral vibration of the rotor is relatively limited. In fact, the lateral vibration of the rotor is caused by both unbalanced electromagnetic force generated by the interaction of electromagnetic fields between stator and rotor and the centrifugal force generated by eccentric rotor. The rotor eccentricity not only causes nonuniform airgap but also further affect the flux configuration and electromagnetic density distribution, so unbalanced electromagnetic force is an inevitable concomitants [8]. In addition, nonuniform airgap makes everchanging electromagnetic resultant of the rotor and in turn changes lateral vibration locus of the rotor which affects airgap redistribution. Modeling and analyzing vibration characteristic of the rotor under complicated electromagnetic force becomes very critical. Meanwhile, the interaction of electromagnetic force and vibration displacement during rotor rotation has also brought difficulties for the study of lateral vibration of the rotor.

Compared with other types of motors, analytical representation of radial electromagnetic force for SRM is rather difficult owing to the nonlinear operation [9, 10]. Yang et al. established analytical formula of single tooth electromagnetic force by equivalent electromagnetic circuit and Maxwell stress method and calculated resultants were verified by finite element numerical simulation [11]. Another analytical model of radial force was also established in consideration of electromagnetic saturation and pole arcs width [12]. A novel analytic electromagnetic radial force model applied to bearingless SRM was proposed in the case of rotor eccentricity, which embodied mathematical relationship of radial electromagnetic forces with run parameters such as stator coil current, position angle, and eccentricity [13]. Weiss et al. gave out the dependency of unbalanced radical electromagnetic force and torque ripple on eccentricity fault and proved the possibility of compensating them via control currents in opposite poles [14]. The radial volume force components are approximately 5% of surface force contributions acting on material boundaries in SRM. Acting volume forces inside conducting coils were deduced to be only of secondary interest [15]. The novel rotor structure and multiobjective optimization method has been used to radical force reduction in order to improve SRM performance [16–18]. These literatures have tremendous contribution to radical force analysis; however, radical electromagnetic resultant model and lateral vibration under this external force during rotor rotating are not carried out adequately.

At present, lateral vibration response of the rotor is studied mainly through numerical simulation. The orbital response was investigated by coupling field method of electromagnetic field and mechanical structure field [19, 20]. It was verified that the rotor's eccentricity is magnified due to vibration effect caused by the unbalanced electromagnetic force [8]. SRM was modeled as a whole machine, and then modal, dynamic, and harmonic analysis was carried out to explore the vibration method of the whole system [21]. These works focused on vibration performance of the rotor in time domain but lack detailed results in frequency domain. Besides, the vibration response under the interaction between the electromagnetic force and the displacement trajectory as well as the lateral superharmonic resonance of the rotor is missing.

In this paper, lateral vibration equation of rotor at constant speed is established by finite element method based on vibration equation of rotating elastic beam and bearing link element. Critical speed and vibration mode of the rotor is obtained through Campbell chart and modal analysis. External force analytic formulas about unbalanced electromagnetic and centrifugal force are deduced in detail, which embodies complicated relation with motor's parameters such as structure sizes, initial eccentricity, and winding currents. Then electromagnetic resultant and vibration displacement of the rotor at rated speed are solved with Newmark-Beta method and their typical characteristics both in time and frequency domain are summarized. Final superharmonic resonance phenomenon of the rotor at some particular speed rotational speed is revealed. These research results will help to better discuss the vibration characteristic of SRM rotor. It

is very beneficial for vibration evaluation and optimization of advanced SRM.

2. Lateral Vibration Equation of Rotor

A 12/8 pole SRM is used in this study. It is mainly comprised of stator core, windings wrapped in stator poles, rotor core without any magnets or coils, and central multistage shaft. The model compositions of SRM and rotor appearance are shown in Figure 1. Rotor's main dimension is listed in Table 1. Two rolling ball bearings with equal orthogonal stiffness and damping are mounted on both sides of the multistage shaft. The material of rotor core is silicon steel and that of central multistage shaft is 45 steel.

Most flexible rotors can be considered as beam-like structures. There are several numerical methods for the dynamic analysis of rotor-bearing systems. The most popular of them is the finite element method (FEA), in which inertia moment, gyroscopic moment, and shear force could be included. We can investigate the dynamic behavior of rotors in shorter time and with lower numerical costs by FEA.

The establishment of lateral vibration equation of the rotor is based on the following assumptions: rotor is composed of multistage rotating beams with different length and cross section. Lateral vibration equation of each section beam was modeled by Timoshenko beam elements with consideration of inertia and gyroscopic moment. Stator deformation displacement is rather small compared to vibration displacement of the rotor, so the stator core is treated as rigid body. Only electromagnetic and centrifugal forces are applied to the rotor as external excitation, and other external forces such as air drag and friction force are negligible.

The rotor is firstly divided into several rotational beam sections. Lateral vibration equation of each section is described by a Timoshenko beam element with 8 free degrees and four of which are shared with the neighbor element. Then, all elements of vibration equation are assembled together to generate the vibration equation of the rotor system. Finally, Critical speed and corresponding modes are obtained by Campbell chart and modal analysis of different speed.

2.1. Lateral Vibration Equation of Elastic Beam. After the total strain energy and kinetic energy is represented with shape functions, lateral vibration equation of each elastic beam element can be created by substituting them into Lagrange's equation. The elastic beam element model is shown in Figure 2(a). Its generalized displacements are two direction deflections and two direction angle deflections x, θ_x, y, θ_y of both endpoint nodes. The generalized displacements of arbitrary cross section in this element are the function of length s and time t .

If structural damping effect is neglected, lateral vibration equation of rotating elastic beam element in matrix form is expressed as follows:

TABLE I: Rotor's main dimension.

Segment number	I	II	III	IV	V	VI	VII	VIII
d(mm)	24	26	30	69.2	69.2	30	26	24
l(mm)	5	15	8	41.4	41.4	8	15	5

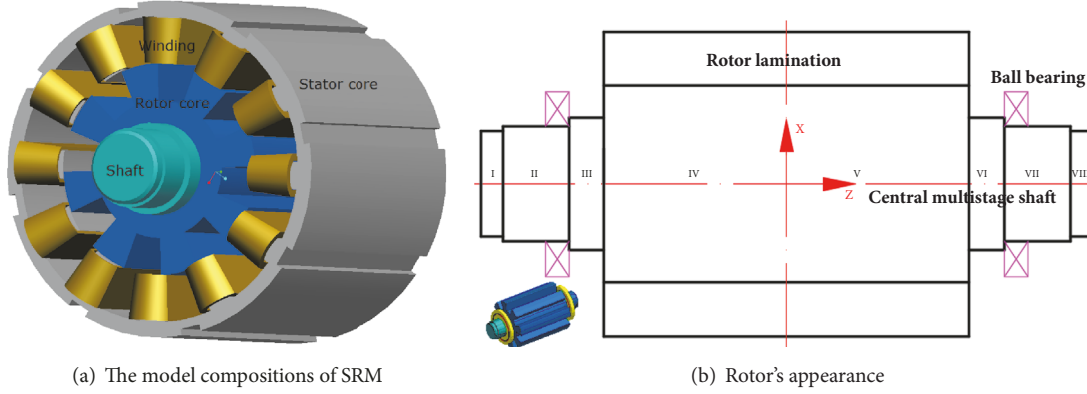


FIGURE 1: Model of SRM and rotor appearance.

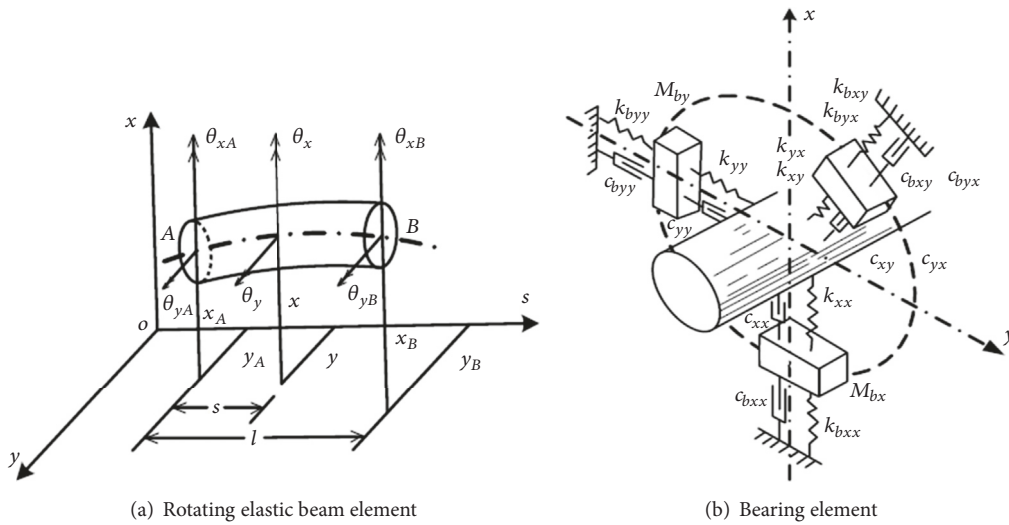


FIGURE 2: Rotating elastic beam element & Bearing element.

$$\begin{aligned}
 & \begin{bmatrix} M_c + \frac{J_s}{2} \\ M_c + \frac{J_s}{2} \end{bmatrix} \begin{bmatrix} \dot{u}_1 \\ \dot{u}_2 \end{bmatrix} + \Omega \begin{bmatrix} J_s \\ -J_s \end{bmatrix} \begin{bmatrix} \dot{u}_1 \\ \dot{u}_2 \end{bmatrix} \\
 & + \begin{bmatrix} K_s \\ K_s \end{bmatrix} \begin{bmatrix} u_1 \\ u_2 \end{bmatrix} = \begin{Bmatrix} Q_1 \\ Q_2 \end{Bmatrix}
 \end{aligned} \quad (1)$$

where $u_1^T = [x_A, \theta_{xA}, x_B, \theta_{xB}]$ and $u_2^T = [y_A, \theta_{yA}, y_B, \theta_{yB}]$ denote generalized displacements of two endpoint nodes. $Q_1^T = [F_{xA}, M_{xA}, F_{xB}, M_{xB}]$ and $Q_2^T = [F_{yA}, M_{yA}, F_{yB}, M_{yB}]$ denote generalized forces corresponding to generalized displacements. M_c, J_s, K_s are mass matrix, gyroscopic matrix, and stiffness matrix of Timoshenko rotational elastic beam element, respectively [22]. Their specific expressions are shown as follows:

$$[M_c] = \frac{\rho A l}{(1 + \phi)^2} \begin{pmatrix} m_1 & m_2 & m_3 & m_4 \\ & m_5 & -m_4 & m_6 \\ & & m_1 & -m_2 \\ \text{sym} & & & m_5 \end{pmatrix}$$

$$[J_s] = \frac{\rho A l}{(1 + \phi)^2} \frac{2I}{A l^2} \begin{pmatrix} m_7 & m_8 & -m_7 & m_8 \\ & m_9 & -m_8 & m_{10} \\ & & m_7 & -m_8 \\ \text{sym} & & & m_9 \end{pmatrix}$$

$$[K_s] = \frac{EI}{l^3 (1 + \phi)} \begin{pmatrix} 12 & 6l & -12 & 6l \\ & l^2 (4 + \phi) & -6l & l^2 (2 - \phi) \\ & & 12 & -6l \\ \text{sym} & & & l^2 (4 + \phi) \end{pmatrix}$$

$$\begin{aligned}
m_1 &= \frac{13}{35} + \frac{7\phi}{10} + \frac{\phi^2}{3} \\
m_2 &= l \left(\frac{11}{210} + \frac{11\phi}{120} + \frac{\phi^2}{24} \right) \\
m_3 &= \frac{9}{70} + \frac{3\phi}{10} + \frac{\phi^2}{6} \\
m_4 &= -l \left(\frac{13}{420} + \frac{3\phi}{40} + \frac{\phi^2}{24} \right) \\
m_5 &= l^2 \left(\frac{1}{105} + \frac{\phi}{60} + \frac{\phi^2}{120} \right) \\
m_6 &= -l^2 \left(\frac{1}{140} + \frac{\phi}{60} + \frac{\phi^2}{120} \right) \\
m_7 &= \frac{6}{5} \\
m_8 &= l \left(\frac{1}{10} - \frac{\phi}{2} \right) \\
m_9 &= l^2 \left(\frac{2}{15} + \frac{\phi}{6} + \frac{\phi^2}{3} \right) \\
m_{10} &= l^2 \left(-\frac{1}{30} - \frac{\phi}{6} + \frac{\phi^2}{6} \right) \\
\phi &= \frac{12EI}{\mu A G l^2}
\end{aligned} \tag{2}$$

where, E denotes elastic modulus of rotor's material, μ denotes Poisson's ratio, ρ denotes density, G denotes shear modulus, and Ω denotes rotational speed of the rotor. l is length of elastic beam element, I is moment of inertia, and A is the area of cross section.

2.2. Lateral Vibration Equation of Bearing Element. Single ball bearing element is simplified as shown in Figure 2(b). It is considered as linear element with constant stiffness and damping, and its lateral vibration equation can be built similar to the vibration in a plane.

The central coordinates of the bearing inner race are defined as x_b and y_b . Corresponding coordinate of beam node is $x_{s(j)}$ and $y_{s(j)}$, respectively. Lateral vibration equation of the ball bearing is expressed as

$$\begin{aligned}
&\begin{bmatrix} M_{bx} & 0 \\ 0 & M_{by} \end{bmatrix} \begin{Bmatrix} \dot{x}_b \\ \dot{y}_b \end{Bmatrix} + \begin{bmatrix} c_{xx} & c_{xy} \\ c_{yx} & c_{yy} \end{bmatrix} \begin{Bmatrix} \dot{x}_b - \dot{x}_{s(j)} \\ \dot{y}_b - \dot{y}_{s(j)} \end{Bmatrix} \\
&+ \begin{bmatrix} k_{xx} & k_{xy} \\ k_{yx} & k_{yy} \end{bmatrix} \begin{Bmatrix} x_b - x_{s(j)} \\ x_b - y_{s(j)} \end{Bmatrix} + \begin{bmatrix} c_{bxx} & c_{bxy} \\ c_{byx} & c_{byy} \end{bmatrix} \begin{Bmatrix} \dot{x}_b \\ \dot{y}_b \end{Bmatrix} \\
&+ \begin{bmatrix} k_{bxx} & k_{bxy} \\ k_{byx} & k_{byy} \end{bmatrix} \begin{Bmatrix} x_b \\ y_b \end{Bmatrix} = \begin{Bmatrix} Q_{1d}^b \\ Q_{2d}^b \end{Bmatrix}
\end{aligned} \tag{3}$$

Assuming $x_b = y_b = 0$, mutual stiffness and mutual damping are ignored. Then equivalent generalized force applied to corresponding beam node can be written as

$$\begin{Bmatrix} Q_{1d}^b \\ Q_{2d}^b \end{Bmatrix} = - \begin{bmatrix} c_x & 0 \\ 0 & c_y \end{bmatrix} \begin{Bmatrix} \dot{x}_{s(j)} \\ \dot{y}_{s(j)} \end{Bmatrix} - \begin{bmatrix} k_x & 0 \\ 0 & k_y \end{bmatrix} \begin{Bmatrix} x_{s(j)} \\ y_{s(j)} \end{Bmatrix} \tag{4}$$

where k_x and k_y denote horizontal and vertical stiffness coefficient of ball bearing and c_x and c_y are damping coefficient, respectively.

2.3. Total Lateral Vibration Equation of the Rotor. The real rotor of SRM is divided into 41 nodes and 40 segment Timoshenko rotating beam elements. Final discretized nodes and elements with rotating elastic beam and bearing elements are shown in Figure 3. The bearing coefficient is applied to corresponding node by its equivalent generalized force. Lateral vibration equation of the rotor-bearing system is axially symmetrical around its spin Z axis, which is expressed in the following general form:

$$M\ddot{q}(t) + (C - \omega G)\dot{q}(t) + Kq(t) = F(q, t) \tag{5}$$

where $q = [x_1, \theta_{x1}, y_1, \theta_{y1}, x_2, \theta_{x2}, y_2, \theta_{y2}, \dots, x_N, \theta_{xN}, y_N, \theta_{yN}]^T$ is a vector containing generalized coordinates, referring to an inertial frame. M is the symmetric mass matrix, C is the symmetric damping matrix, G is the skew-symmetric gyroscopic matrix, and K is the symmetric stiffness matrix. Bearing stiffness and damping is embodied in C and K . They are all diagonal band sparse matrix with size of 164 by 164. $F(q, t)$ is a generalized force vector dependent on time t and intermediate displacement q , in which all force functions are listed.

If (5) is expanded, we can get the total lateral equation of vibration expressed by a detailed matrix form as follows:

$$\underbrace{\begin{bmatrix} M_1 & \dots & & \\ & \dots & & \\ & & \dots & \\ & & & \dots \\ & & & & \dots & M_{40} \end{bmatrix}}_M \begin{Bmatrix} \ddot{q}_1 \\ \vdots \\ \ddot{q}_{81} \\ \cdot \\ \ddot{q}_{83} \\ \vdots \\ \ddot{q}_{164} \end{Bmatrix}$$

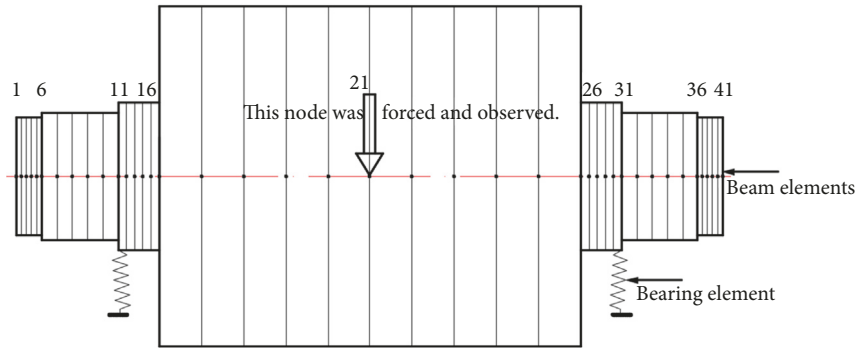


FIGURE 3: Nodes and elements with Timoshenko beam elements.

$$\begin{aligned}
 & + \underbrace{\begin{pmatrix} C_1 & \dots & \dots \\ \vdots & \ddots & \vdots \\ \dots & \dots & C_{40} \end{pmatrix}}_C \\
 & - \omega \underbrace{\begin{pmatrix} G_1 & \dots & \dots \\ \vdots & \ddots & \vdots \\ \dots & \dots & G_{40} \end{pmatrix}}_G \begin{Bmatrix} \dot{q}_1 \\ \vdots \\ \dot{q}_{81} \\ \cdot \\ \dot{q}_{83} \\ \vdots \\ \dot{q}_{164} \end{Bmatrix} \\
 & + \underbrace{\begin{pmatrix} K_1 & \dots & \dots \\ \vdots & \ddots & \vdots \\ \dots & \dots & K_{40} \end{pmatrix}}_K \begin{Bmatrix} q_1 \\ \vdots \\ q_{81} \\ \cdot \\ q_{83} \\ \vdots \\ q_{164} \end{Bmatrix} \\
 & = \begin{Bmatrix} 0 \\ \vdots \\ Fux + Fmx \\ \cdot \\ Fuy + Fmy \\ \vdots \\ 0 \end{Bmatrix}
 \end{aligned}$$

(6)

The external forces of the rotor include the radical electromagnetic unbalanced force generated by the interaction between stator and rotor, as well as the centrifugal force generated by rotor eccentricity. They are applied onto intermediate node in the form of concentrated force. Note that the external forces are the function of vibration displacement and time; thus the total equation of the rotor becomes a typical nonlinear question.

2.4. Campbell Chart and Whirl Critical Speed. Under fairly wide assumptions, lateral behavior of a beam can be considered uncoupled from its axial and torsional behavior. When flexural behavior can be uncoupled from axial and torsional ones, (6) holds for flexural behavior [23]. After Z displacement U_z and rotation angle around Z axis Rot_z are constrained, freedom degrees of every node are reduced to 4, i.e., x displacement and rotation angle around x axis, y displacement and rotation angle around y axis, denoted by $U_x, U_y, Rot_x,$ and Rot_y . Two linear spring damping elements in orthogonal direction are used to replace the bearings. Mechanical properties of the rotor and bearing coefficients are shown in Table 2.

Campbell chart of the rotor was drawn through mode analysis at different rotational speeds, as shown in Figure 4. Critical speed analysis does not involve material damping. In Campbell chart, oblique line shows various excitation forces. Positive precession curve is an upper branch while negative is a lower branch. The intersection between oblique line and every pair precession curves are just forward and backward critical rotational speed. Usually, only forward whirl critical rotational speeds under synchronous are considered when calculating critical speed. Their specific values are obtained through the intersection points by program automated selected.

The first four-order forward critical speeds of the rotor are listed in Table 3 and their corresponding critical modes are shown in Figure 5. Due to the symmetry of the rotor structure and equal parameters of the bearing in orthogonal direction, the critical modes are also symmetric. The first forward critical speed 1,357.9 Hz of rotor is far more than rated speed 3,000 rpm of the rotor. The gyroscopic effect of the rotor is not prominent because there is no big inertial disc on the rotor. First-order critical speed is almost not affected by rotational speed when the rotor runs.

TABLE 2: Material properties of the rotor and bearing coefficients [24].

Component	Material	Density ρ	Elasticity modulus E	Poisson's ratio μ
Rotor	steel	7850 kg/m ³	220 GPa	0.3
Bearing	Horizontal stiffness	Vertical stiffness	Horizontal damping	Vertical damping
	k_x 10 ⁸ N/m	k_y 10 ⁸ N/m	c_x 235 N•s/m	c_y 235 N•s/m

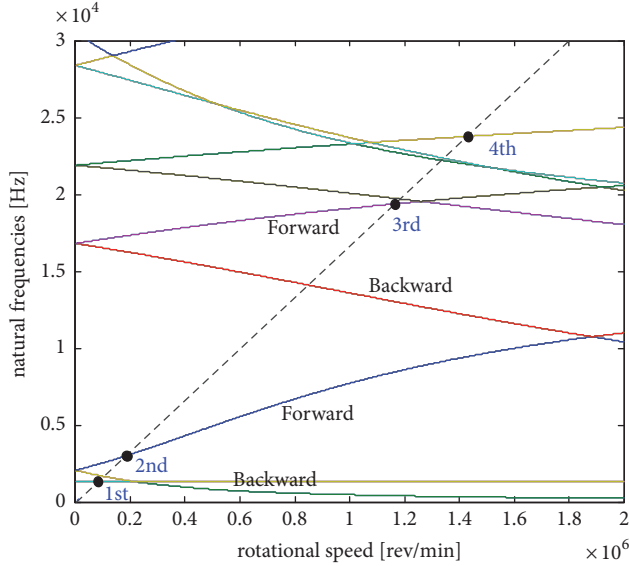


FIGURE 4: Rotor's Campbell chart and the critical speed.

TABLE 3: Critical rotational speed of rotor.

Order number	Critical speed (Hz)
1 st	1,357.9
2 nd	2,947.83
3 rd	19,370.55
4 th	23,759.11

Conical vibration mode above second critical speed could be avoided if the ratio between the transverse and the polar mass moments of the rotor is suitably small. We focus on the superharmonic vibration of the rotor when it is far below the rated speed. Therefore, the rotor can be used as a rigid rotor for the following further study.

3. External Excitation Forces of the Rotor

The initial eccentricity of the rotor will cause a centrifugal force and an unbalanced electromagnetic force because of uneven airgap distribution between the stator and rotor teeth. When they are applied onto intermediate node of the rotor, the rotor will generate transverse vibration.

3.1. Centrifugal Force of Rotor. The unbalance force vector can be described as a vector rotating with the same angular speed as the rotor. In the stationary XOY system, the rotation schematic of eccentric rotor is shown in Figure 6. The rotor

rotates around stator central axis O. E axis is the instantaneous axis of the rotor. Horizontal and vertical vibration displacements are defined as u_x and u_y , respectively; i.e., the distance of central axis E deviated from central axis O.

When the rotor runs at constant speed ω , the centrifugal force components in x-y plane is expressed as follows:

$$\begin{aligned}
 F_{ux} &= m \sqrt{[u_x + \varepsilon \sin(\omega t)]^2 + [u_y + \varepsilon \cos(\omega t)]^2} \omega^2 \\
 &\quad \cdot \cos(\omega t + \beta_{\text{int}}) \\
 F_{uy} &= m \sqrt{[u_x + \varepsilon \sin(\omega t)]^2 + [u_y + \varepsilon \cos(\omega t)]^2} \omega^2 \\
 &\quad \cdot \sin(\omega t + \beta_{\text{int}}) \\
 \beta_{\text{int}} &= \arctan\left(\frac{u_y + \varepsilon}{u_x}\right)
 \end{aligned} \quad (7)$$

where m denotes the mass of lamination segment, ε denotes initial distance between the barycenter axis G and the axis E, and β_{int} denotes initial eccentric angle. Obviously, (7) is the function of vibration displacement and initial eccentricity.

3.2. Radical Electromagnetic Force of Rotor. Radial electromagnetic force generated by single coil near aligned position is much larger than the tangential force, and the lateral vibration of the rotor is mainly caused by the radial force [8], so just radical force is considered. Due to magnetic permeability of silicon steel being much larger than that of airgap, magnetic line is almost vertical in the surface of stator and rotor [13, 14]. According to the Maxwell stress method, radial force of a rotor's tooth suffered in the electromagnetic field is independent of integration path.

If we interrupt stator yoke section located at both side of stator tooth as a boundary and choose integral path as closed solid line as shown in Figure 7, then magnetic density will be divided into two parts, main magnetic density of overlapping parts and fringing magnetic density of nonoverlapping parts. By magnetic density integral along respective path and sum, the radial electromagnetic force of rotor's single tooth is expressed as follows:

$$\begin{aligned}
 F_{sr} &= \frac{h}{2\mu_0} \left(\int_1^2 B_{f1}^2 dl + \int_2^3 B_m^2 dl + \int_4^5 B_m^2 dl + \int_5^6 B_{f2}^2 dl \right) \\
 &= \frac{h}{2\mu_0} [B_{f1}^2 l_{12} + B_m^2 (l_{23} + l_{45}) + B_{f2}^2 l_{56}]
 \end{aligned} \quad (8)$$

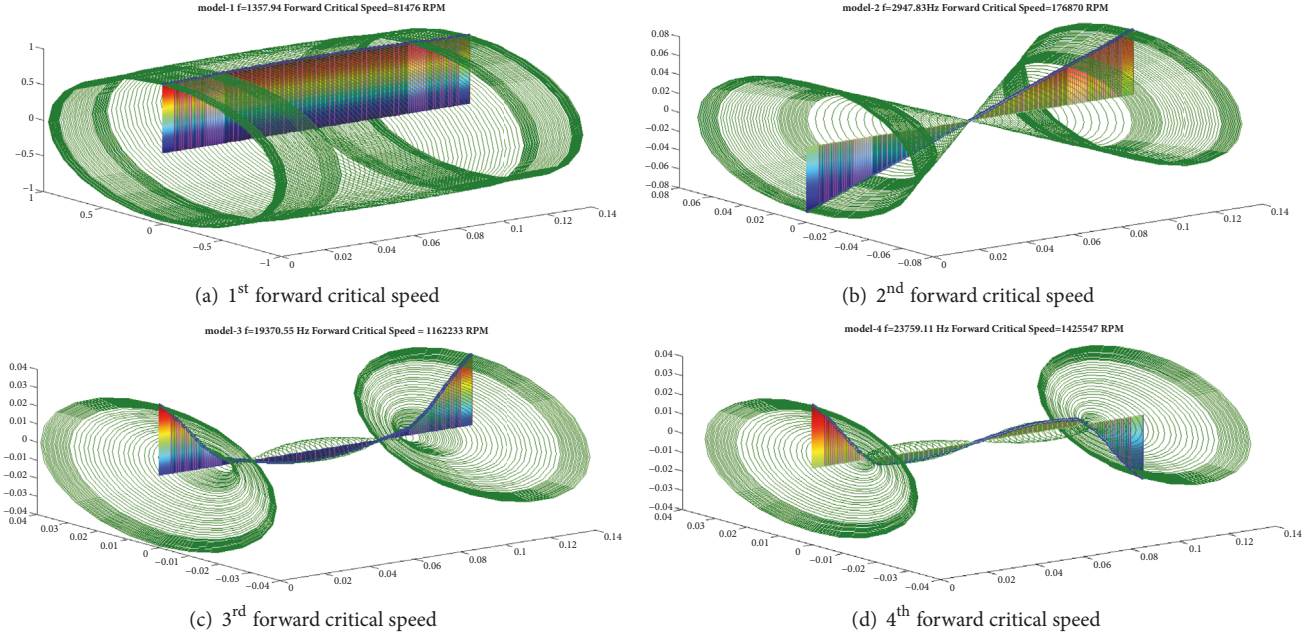


FIGURE 5: The first four-order forward critical speeds and corresponding modes.

where h is laminated length of the rotor, μ_0 is air permeability, B_m is main airgap magnetic density of overlapping parts, and B_{f1} and B_{f2} are two fringing magnetic density of nonoverlapping parts, respectively.

Two fringing magnetic densities appear close to symmetry, i.e., $B_{f1} \approx B_{f2}$ [14]. Main and fringing magnetic densities are calculated through BH curve by equivalent magnetic circuit method [11]. After substituting them into (8), the single tooth radial force formula of the rotor is finally converted into

$$\begin{aligned}
 F_{sr}(l_0, i, \beta) = & \frac{h\mu_0}{2} \left\{ \frac{1}{l_0^2} \left[U \left(1 - \frac{1}{2e_m} \right) + \frac{l_m B_{sat}}{2\mu} \right. \right. \\
 & - \left. \left. \sqrt{\frac{l_m^2 B_{sat}^2}{4\mu^2} + U \frac{B_{sat}}{e_m \mu} \left(l - \frac{l_m}{2} \right) + \frac{U^2}{4e_m^2}} \right]^2 \left(\frac{\pi r}{12} \right. \right. \\
 & - r |\beta| \left. \right) + \frac{1}{l_{f1}^2} \left[U \left(1 - \frac{1}{2e_f} \right) + \frac{l_f B_{sat}}{2\mu} \right. \\
 & - \left. \left. \sqrt{\frac{l_f^2 B_{sat}^2}{4\mu^2} + U \frac{B_{sat}}{e_f \mu} \left(l - \frac{l_f}{2} \right) + \frac{U^2}{4e_f^2}} \right] (l_0 \right. \\
 & \left. \left. + 2r |\beta| \right) \right\} \quad (9)
 \end{aligned}$$

where $U = N_m \cdot i$, $\mu = \mu_0 \mu_r$, $e_m = 1 + l_0/l$, $l_m = l + \mu l_0 / e_m \mu_0$, $e_f = 1 + l_{f1}/l$, and $l_f = l + \mu l_{f1} / e_f \mu_0$.

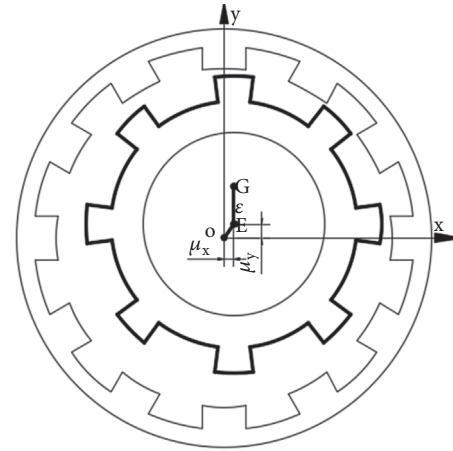


FIGURE 6: Rotation schematic of eccentric rotor.

μ is the silicon steel permeability. l_0 is airgap length. U is the magnetomotive force. N_m is coil turns. i is coil current. β is overlapping arc between stator and rotor. l_m is the mean length of main airgap. l_{f1} is the mean length of fringing airgap and expressed as $l_{f1} = l_0 + \pi r |\beta| / 4$ assumed that magnetic force line is circular arc.

Primary technical parameters of 12/8 pole SRM are given in Table 4. When they are substituted into (9), final single tooth radial electromagnetic force of the rotor under single coil energized can be obtained.

In most cases, the rotor generates eccentricity because of manufacture or installation issues. The radical electromagnetic force of the rotor's opposite teeth is no longer balanced when one phase winding energized. Initial eccentric distance

TABLE 4: Primary technical parameters of 12/8 pole SRM.

Parameter	Definition	Value
N_s	Number of stator pole	12
N_r	Number of rotor pole	8
h	Stack length	82.8 [mm]
D_{so}	Outer diameter of stator	120 [mm]
D_{si}	Inner diameter of stator	69.8 [mm]
D_{ro}	Outer diameter of rotor	69.3 [mm]
D_{ri}	Inner diameter of rotor	30 [mm]
l_0	Airgap length	0.25 [mm]
l	Length between stator & rotor yoke	34.45 [mm]
τ	Pole arc of stator and rotor	15°
N_m	Turns of each pole coil	50
μ_0	Permeability of air	$4\pi \times 10^{-7}$ [H/m]
μ_r	Relative permeability of silicon steel	5000
B_{sat}	Saturated magnetic density	2.2 [T]
P	Rated power	3 [kW]
n_0	Rated speed	3000 [r/min]

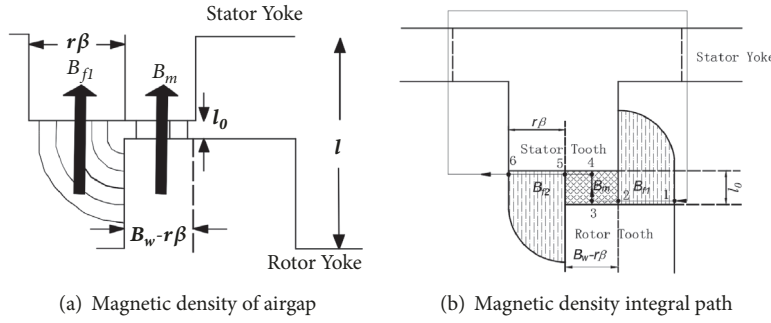


FIGURE 7: Magnetic density of airgap and integral path [11].

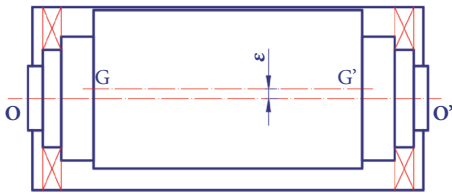


FIGURE 8: Definition of rotor eccentricity ratio.

of lamination segment is ϵ and its ratio to l_0 is defined as eccentricity ratio, as shown in Figure 8.

The opposite two coils located on a π radians displacement are connected to form one phase and SRM runs by six-phase mode. Six-phase windings are energized by ideal square wave currents in sequence. Winding currents and radial electromagnetic resultant of the eccentric rotor with rotation angle are shown in Figure 9. Note that radial electromagnetic force generated by radial eccentricity along the radius is far greater than that generated by tangential eccentricity perpendicular to the radius [20]; thus radial electromagnetic force induced by radial eccentricity is primary. According to rotation angle, instantaneous radial

eccentricity, and energized current, horizontal and vertical electromagnetic resultants of the rotor could be obtained by decomposition of opposite teeth radial force. Its specific expression is as follows:

$$F_m = F_{sr} \left(l_{01}, i, \frac{2\pi n}{2N_s} - \theta \right) - F_{sr} \left(l_{02}, i, \frac{2\pi n}{2N_s} - \theta \right)$$

$$F_{mx} = F_m \cdot \cos \left[\theta + \frac{2\pi(2-n)}{n_r} \right]$$

$$F_{my} = F_m \cdot \sin \left[\theta + \frac{2\pi(2-n)}{n_r} \right]$$
(10)

$$\frac{2(n-1)\pi}{2N_s} \leq \theta < \frac{2n\pi}{2N_s}, \quad n \in \text{int}[1 : 1 : 24]$$

where l_{01} and l_{02} are two opposite instantaneous airgap between rotor and stator tooth, expressed as

$$l_{01} = l_0 \left[1 - \epsilon \cdot \cos \left(\frac{n\pi}{4} \right) \right] - \mu_x \cos \left[\theta + \frac{(2-n)\pi}{4} \right]$$

$$- \mu_y \sin \left[\theta + \frac{(2-n)\pi}{4} \right]$$

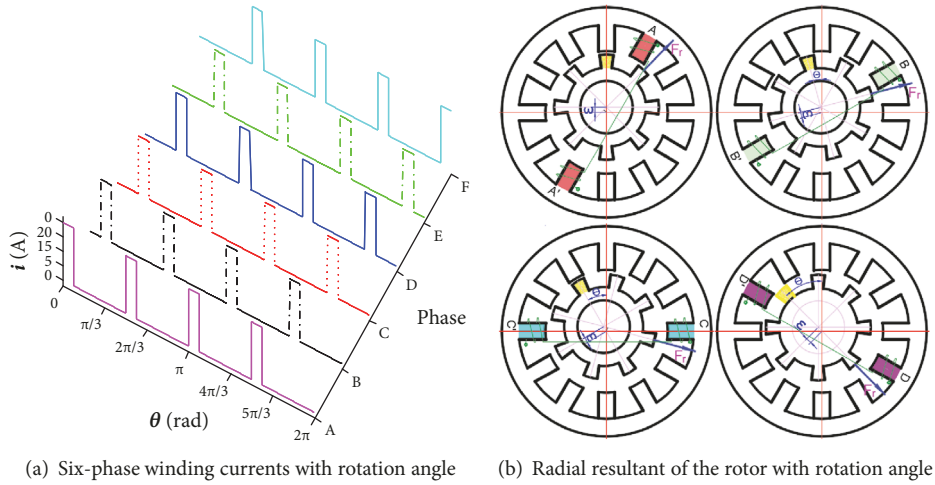


FIGURE 9: Winding currents and radial electromagnetic resultant.

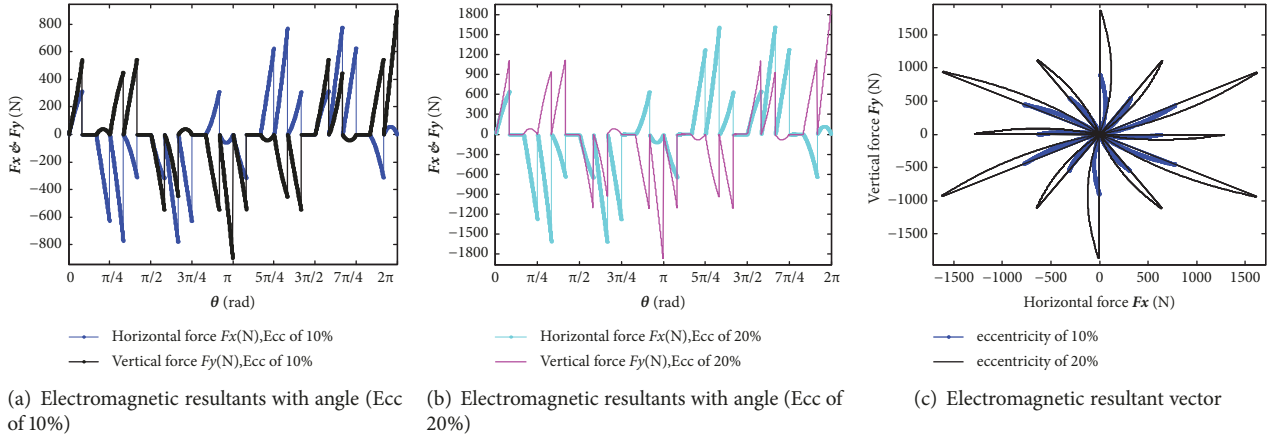


FIGURE 10: Electromagnetic resultant and electromagnetic resultant vector.

$$\begin{aligned}
 l_{02} = l_0 & \left[1 + \varepsilon \cdot \cos\left(\frac{n\pi}{4}\right) \right] + \mu_x \cos\left[\theta + \frac{(2-n)\pi}{4}\right] \\
 & + \mu_y \sin\left[\theta + \frac{(2-n)\pi}{4}\right]
 \end{aligned} \quad (11)$$

Among them, F_{sr} is radical electromagnetic force of single rotor tooth in (9) and N_s and N_r are the numbers of stator teeth and rotor teeth, respectively. θ is rational angle of the rotor. Both u_x and u_y denote horizontal and vertical displacement of rotor's intermediate node.

Figure 10 shows the horizontal and vertical electromagnetic resultants of the rotor with rotation angle as well as electromagnetic resultant vector. These results were done with eccentric distance ε in direction set as 0.025mm and 0.05mm (i.e., eccentricity ratio of 10% and 20%) without any interaction between resultant and vibration displacement of the rotor.

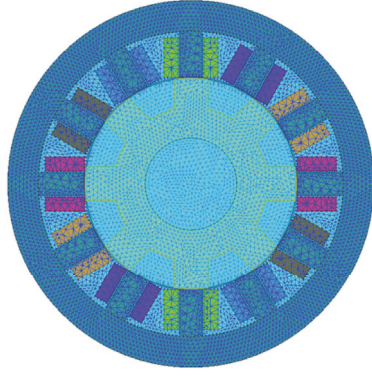
Moreover, we also use Maxwell software to simulate radial electromagnetic resultant of the rotor under the rated

speed. The FEM mesh, drive control circuit, horizontal electromagnetic resultant contrast both in time and frequency and resultant vector contrast are shown in Figure 11. Their consistency verifies the validity of formula (10). The small difference is mainly attributed to the neglect of airgap caused by tangential eccentricity.

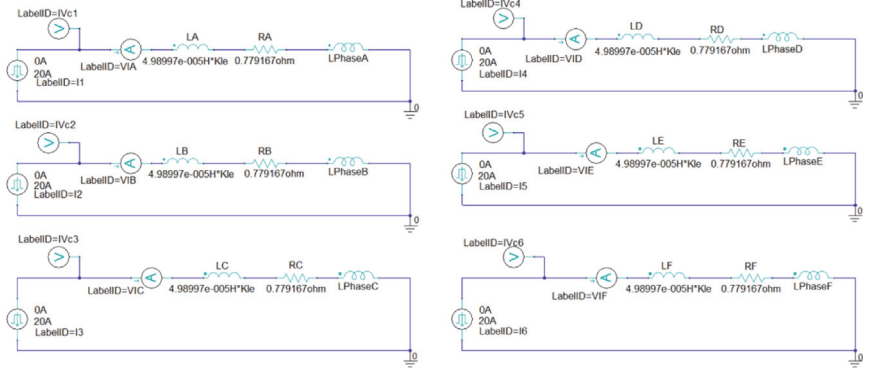
Unfortunately, it is very difficult to test directly and accurately the electromagnetic resultant force, which is limited to our current experimental conditions. So far, there are few literatures which give rough experimental measurement results of radical electromagnetic force [25, 26]. When calculating the rotor lateral vibration displacement, unbalance external resultants of rotor need to be solved in time according to winding current, rotation angle, and actual airgap and are applied onto the intermediate node of the rotor.

4. Forced Lateral Vibration Response at Rated Speed

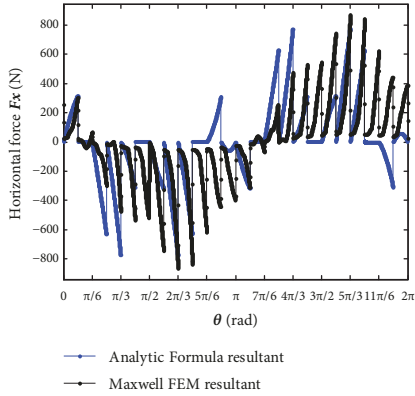
After total vibration equation of the rotor is generated and external resultants are applied onto intermediate nodes,



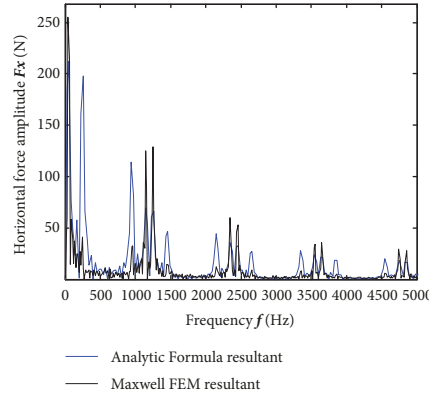
(a) Maxwell FEM mesh of SRM



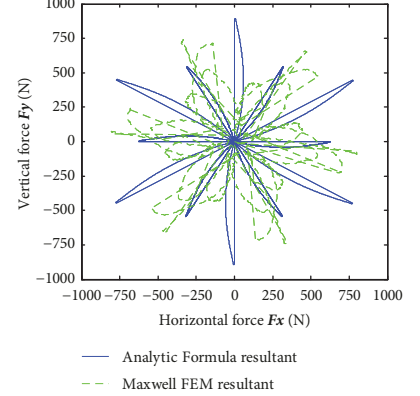
(b) Drive control circuit to produce ideal square current



(c) Time course contrast of horizontal resultant



(d) Amplitude spectrum contrast of the horizontal resultant



(e) Resultant vector contrast

FIGURE 11: The contrast of electromagnetic resultant with analytic and FEM.

vibration displacement response could be calculated by the Newmark-Beta numerical method. Vibration results of the intermediate node are extracted for intensive study.

4.1. Calculation Process of Vibration Displacement Response. Under the action of external excitation forces, the vibration response analysis of the rotor is calculated as follows [27]:

(1) Form the mass matrix $[M]$, damping matrix $[C]$, gyro matrix $[G]$ and stiffness matrix $[K]$, and generate lateral vibration equation;

(2) Giving out initial rotor's displacement u_0 and velocity \dot{u}_0 at initial time t_0 , the resultant Q_0 including both centrifugal and electromagnetic resultants is loaded onto the intermediate node of the rotor, and then calculate the acceleration \ddot{u}_0 ;

(3) Select time step Δt and parameter β and γ , and calculate integral constant:

$$c_0 = \frac{1}{\beta(\Delta t)^2},$$

$$c_1 = \frac{\gamma}{\beta(\Delta t)},$$

$$c_2 = \frac{1}{\beta(\Delta t)},$$

$$c_3 = \left(\frac{1}{2\beta} - 1 \right)$$

$$c_4 = \frac{\gamma}{\beta} - 1,$$

$$c_5 = \left(\frac{\gamma}{2\beta} - 1 \right) (\Delta t),$$

$$c_6 = (1 - \gamma) (\Delta t),$$

$$c_7 = \gamma (\Delta t)$$

(12)

(4) Form the effective stiffness matrix \widehat{K} ;

$$\widehat{K} = K + c_0 M + c_1 (C - \omega G) \quad (13)$$

(5) Recomputed the resultant $Q_{t+\Delta t}$ in (7) and (10) with changed airgap, winding real excitation current and rotational angle, and then calculate equivalent load $\widehat{Q}_{t+\Delta t}$ at the time of $t + \Delta t$;

$$\widehat{Q}_{t+\Delta t} = Q_{t+\Delta t} + (c_0 u_t + c_2 \dot{u}_t + c_3 \ddot{u}_t) M + (c_1 u_t + c_4 \dot{u}_t + c_5 \ddot{u}_t) (C - \omega G) \quad (14)$$

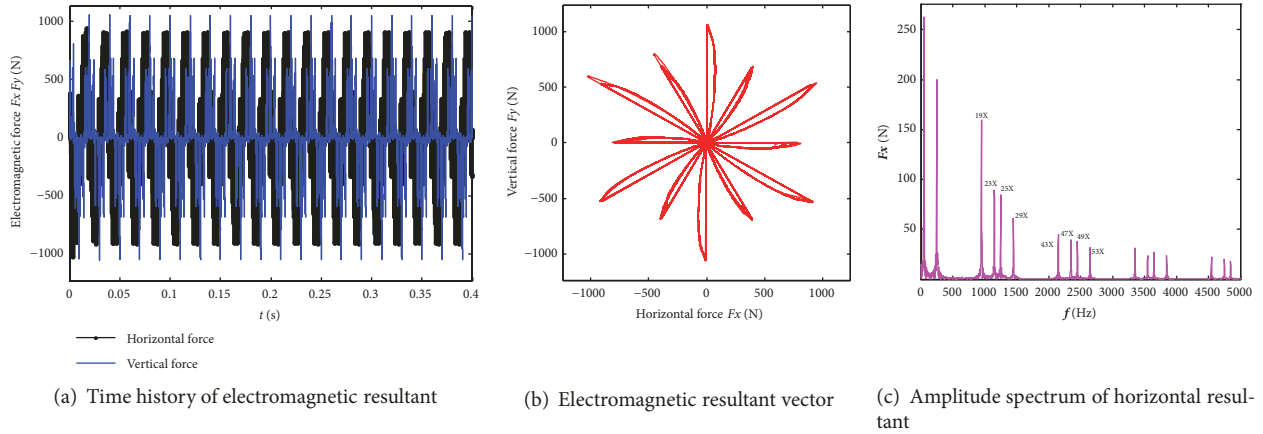


FIGURE 12: Time history of electromagnetic resultant at rated speed.

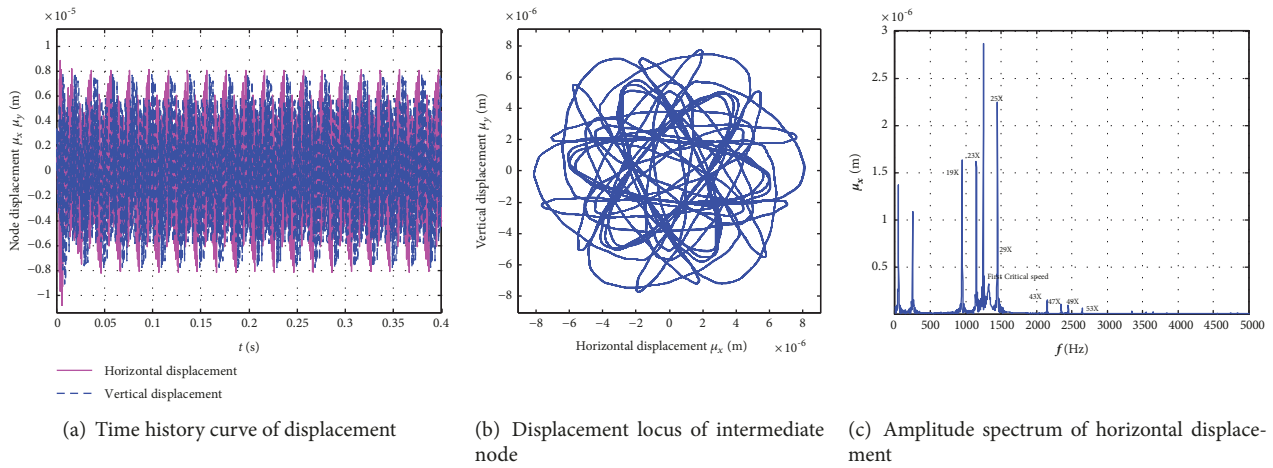


FIGURE 13: Time history of vibration displacement at rated speed.

(6) Solve the displacement at the time of $t + \Delta t$;

$$\mathbf{u}_{t+\Delta t} = \widehat{\mathbf{K}}^{-1} \widehat{\mathbf{Q}}_{t+\Delta t} \quad (15)$$

(7) Calculate the acceleration and velocity at $t + \Delta t$;

$$\begin{aligned} \ddot{\mathbf{u}}_{t+\Delta t} &= c_0 (\mathbf{u}_{t+\Delta t} - \mathbf{u}_t) - c_2 \dot{\mathbf{u}}_t - c_3 \ddot{\mathbf{u}}_t \\ \dot{\mathbf{u}}_{t+\Delta t} &= \dot{\mathbf{u}}_t + c_6 \ddot{\mathbf{u}}_t + c_7 \ddot{\mathbf{u}}_{t+\Delta t} \end{aligned} \quad (16)$$

When $\gamma \geq 0.5$, $\beta \geq 0.25(\gamma + 0.5)^2$, Newmark-Beta numerical integral method is unconditional stable [28]. That is, the time step Δt does not affect the stability of the solution. Hence, the selection of Δt is dependent on the accuracy of the solution and determined by maximum period of several natural modes which greatly contributed to the response. In most cases, it is usually selected as one fraction of minimum natural vibration period. The corresponding period of first-order critical speed was considered in there and Δt was selected less than its 1/20.

4.2. Vibration Locus of Rotor at Rated Speed. At rated speed of 3,000 rpm, the vibration displacement of the rotor was

simulated in set time range. Time history curve of electromagnetic resultant, the resultant vector, and amplitude spectrum of the resultant is shown in Figure 12. Time history curve of vibration displacement, the displacement vector, and amplitude spectrum of the displacement is shown in Figure 13. It can be seen that the rotor vibration locus is distributed in a circular domain after steady state, and vibration displacement of intermediate nodes is also periodic because of periodic electromagnetic resultant.

The maximum lateral displacement of the rotor is not more than 0.01 mm, which is far less than the design gap between the stator teeth and rotor teeth. The stator and rotor will not collide during rotor's operation. The rotor could run stably at the rated speed, which is consistent with actual operation conditions.

Electromagnetic resultant of the rotor after the steady state is periodic. Current duty ratio is 1:5 in square wave current of each phase winding, and every phase winding is energized 4 times in order during one round rotation. Thus, amplitude spectrum of electromagnetic resultant shows that multifrequency and main frequency are distributed in several frequency bands. The lowest frequency components

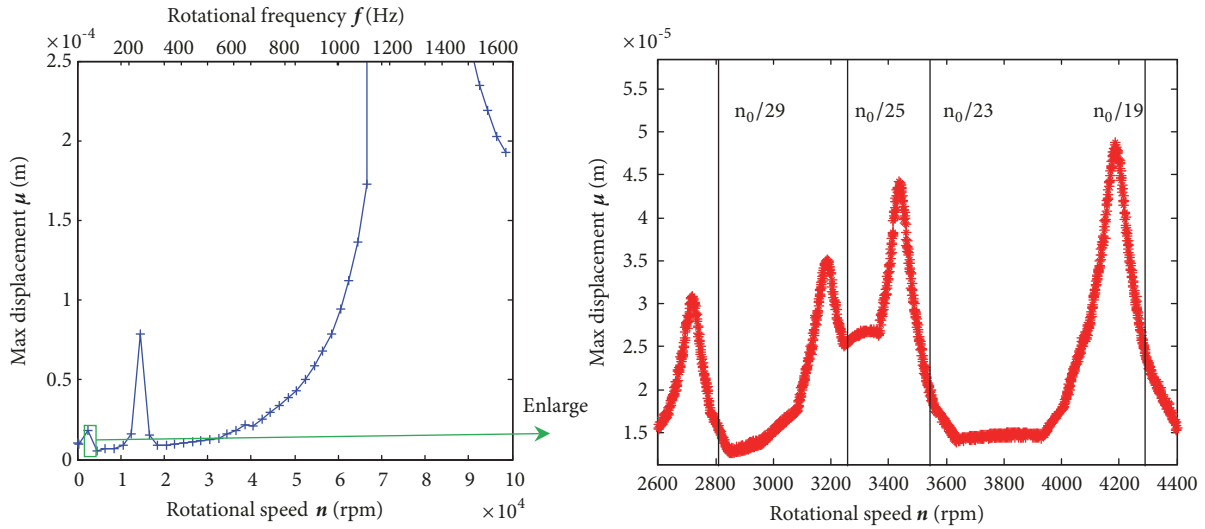


FIGURE 14: Maximum vibration displacement with rotation speed.

are the fundamental frequency X and fifth harmonic $5X$, and the rest frequency components are distributed in both sides of integral multiple current switch frequency. The first band group is 24 times harmonics group, i.e., $19X$, $23X$, $25X$, and $29X$; the second band group is 48 times harmonics group, i.e., $43X$, $47X$, $49X$, and $53X$; the third band group is 72 times harmonics group, i.e., $67X$, $71X$, $73X$, and $77X$. These frequency components ascend in proper sequence and form energy intensive multiple frequency bands.

The frequency components of the horizontal displacement are relatively simpler compared to that of the horizontal resultant and mainly distributed in the frequency range ahead of the first-order critical speed. The frequency amplitude near the first-order critical rotational speed is relatively larger. The energy after the first-order critical speed is suppressed so that the amplitude reduced significantly.

Through the detailed analysis of electromagnetic resultant and vibration displacement in frequency domain, we prove that lateral vibration frequency distribution is related to rotational speed, current switch frequency and wave. The least common multiple of the number of poles in rotor and stator is 24. The duty ratio of each phase current is 1:5. So frequency distribution in electromagnetic resultant spectrum is related to the frequency of X , $5X$, and $24 * k * X \pm X$, $24 * k * X \pm 5X$. However, frequency distribution in displacement spectrum is closely related not only to them but also to the first-order forward critical speed of the rotor.

The first-order critical rotation speed of the rotor exits in the horizontal displacement spectrum but does not appear in the horizontal resultant spectrum. It proves that the effect of vibration displacement on electromagnetic resultant is weak. Lateral vibration displacement only causes uneven airgap redistribution and modulates the resultant electromagnetic resultant. Therefore, electromagnetic resultant edge frequency shows an obvious asymmetry.

5. Lateral Superharmonic Resonance of the Rotor

Rotor's rotational speed could change the external resultant of the rotor and also affect the gyro matrix of whole lateral vibration equation. The lateral vibrations of the rotor under different rotation speed are resolved circularly. The lateral maximum vibration displacement of intermediate node on the rotor is shown in Figure 14. Since lateral maximum displacement of the rotor is relatively larger in the range of 2,600-4,400 rpm, the maximum displacement is solved within finer range of rotational speeds.

From Figure 14, it is clear that the resonance response of the rotor will occur when the rotor runs at the rotational speed near the first-order critical speed. At this point, the maximum displacement of intermediate node exceeds the airgap length of 0.25mm. There will be a collision between the rotor and stator. The stator and rotor teeth touch and the rotor cannot run normally. Therefore, the rotor should avoid running near the first-order critical speed or accelerating over the first-order critical rotational speed into the higher speed.

In addition, the vibration displacement of the rotor is relatively larger when certain harmonic frequency is approximately equal to first-order critical rotational speed of the rotor. Because electromagnetic resultant and vibration displacement of the rotor affect each other, lateral superharmonic resonance of the rotor appears in the rotor.

When the rotor runs at the speed of $1/29$ (2,809.4 rpm) of the first-order critical speed, lateral electromagnetic resultant and lateral displacement of the rotor are simulated. The time history of electromagnetic resultant, steady electromagnetic resultant vector, and amplitude spectrum of horizontal resultant on intermediate node are shown in Figure 15. The corresponding results of lateral displacement are shown in Figure 16.

It can be seen that the frequency components of horizontal electromagnetic resultant are distributed in several

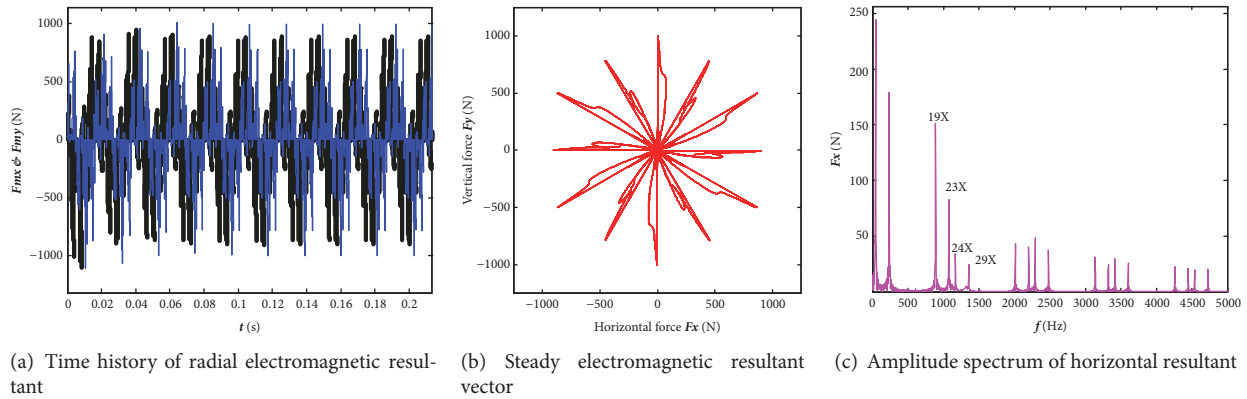


FIGURE 15: Stimulated electromagnetic resultant at 1/29 (2,809.4 rpm).

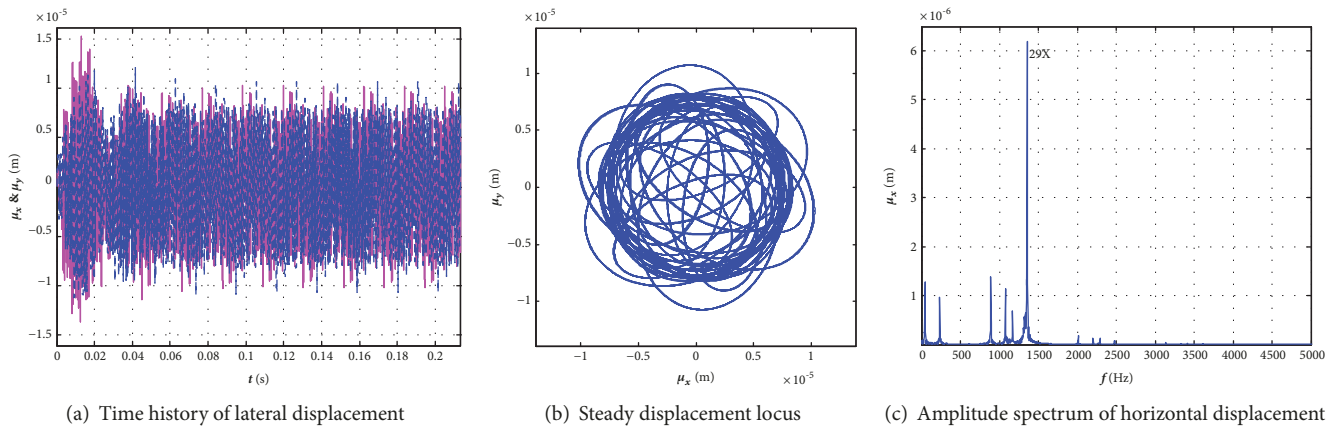


FIGURE 16: Time history, steady locus and amplitude spectrum at 1/29 (2,809.4 rpm).

frequency bands. But the frequency components of lateral displacement are mainly distributed in ahead of the first-order critical rotational speed. The frequency components after first-order critical rotational speed are significantly inhibited. The 29X harmonic frequency component is almost equal to the first-order critical speed of the rotor, and its corresponding amplitude in spectrum is the largest so that the superharmonic resonance happens.

When the rotor runs at the other three superharmonic speeds of 1/25 (3,259.2 rpm), 1/23 (3,542.6 rpm), or 1/19 (4,288.4 rpm) of the first-order critical speed located at the range of 24 times frequency group, each displacement locus of the rotor is simulated, respectively. Steady displacement locus and amplitude spectrum of horizontal displacement are shown in Figure 17.

From Figure 17, lateral steady locus of the rotor at superharmonic speed is markedly different and shows rich diversity. Lateral superharmonic resonance appears at these four speeds. The amplitude of harmonic component which nearly equals the first-order critical speed is maximal in displacement spectrum. This frequency component contributes mostly to lateral vibration.

It is particularly important to note that a similar result could also be obtained as shown in Figure 18, if we solved the rotor locus and carry out spectrum analysis at other superharmonic speed of other harmonics groups such as

48 and 72 times. It will increase more diversity to lateral displacement locus.

In the range of 24 times frequency groups, i.e., the rotational speed from 2,600 rpm to 4,400 rpm, time history of electromagnetic force, and displacement, are solved and spectrum results are transformed into order spectrum. Order spectrum contour of horizontal resultant and horizontal displacement are shown in Figure 19.

From Figure 19, we found that when the rotor rotational speed is 1/19 of the first-order critical speed, amplitude of horizontal displacement is maximal in 19X harmonic frequency which almost equals to the first critical speed. Meanwhile, the amplitude of other harmonic frequency components is very small. The rotor superharmonic resonance happens at this speed. The spectrum distribution of horizontal displacement is similar at other superharmonic speeds. Lateral eccentricity of the rotor at superharmonic speed will be aggravated violently, which probably lead to touch between the rotor and the stator. Therefore, the rotor is best not to run at superharmonic speed for a long time.

6. Conclusion

In this paper, lateral vibration equation of the rotor under constant rotational speed is established by means of finite element method based on a 12/8 poles switched reluctance

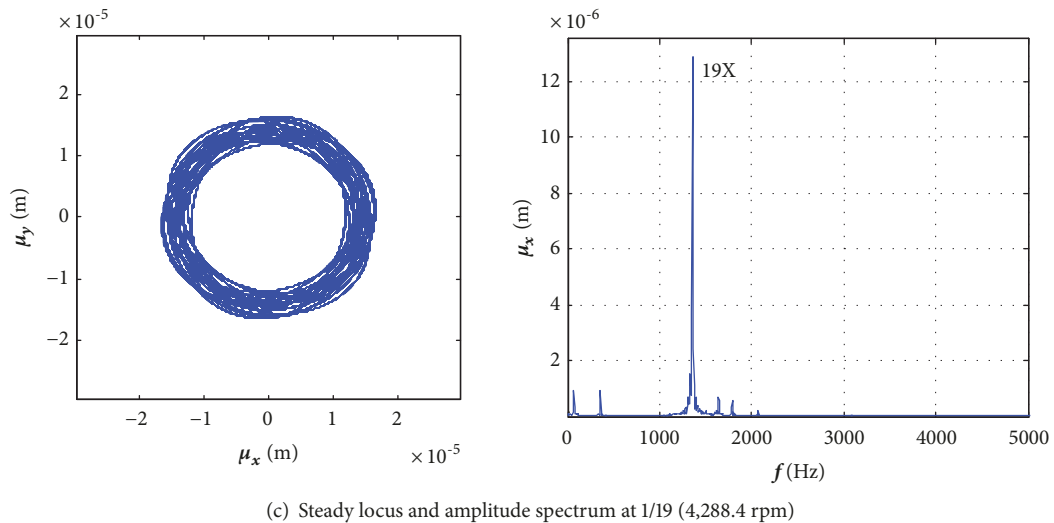
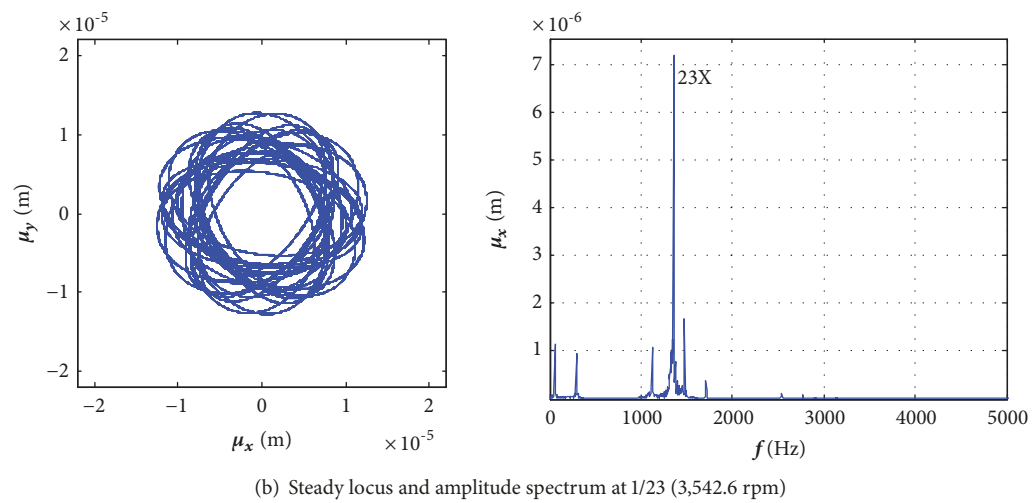
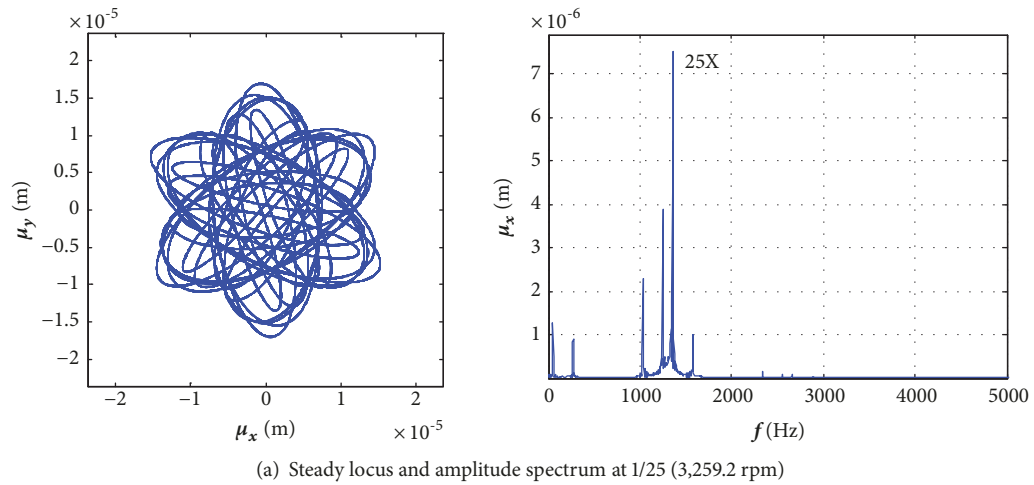


FIGURE 17: Displacement locus and horizontal displacement spectrum.

motor. The expressions of centrifugal force and electromagnetic force of the rotor are derived in detail. The critical speed of the rotor is obtained through the Campbell diagram. In consideration of the interaction between

electromagnetic force and displacement, the lateral vibration response of the rotor is simulated and the spectral characteristics are analyzed. At some specific speed, lateral superharmonic resonance phenomenon of the rotor was

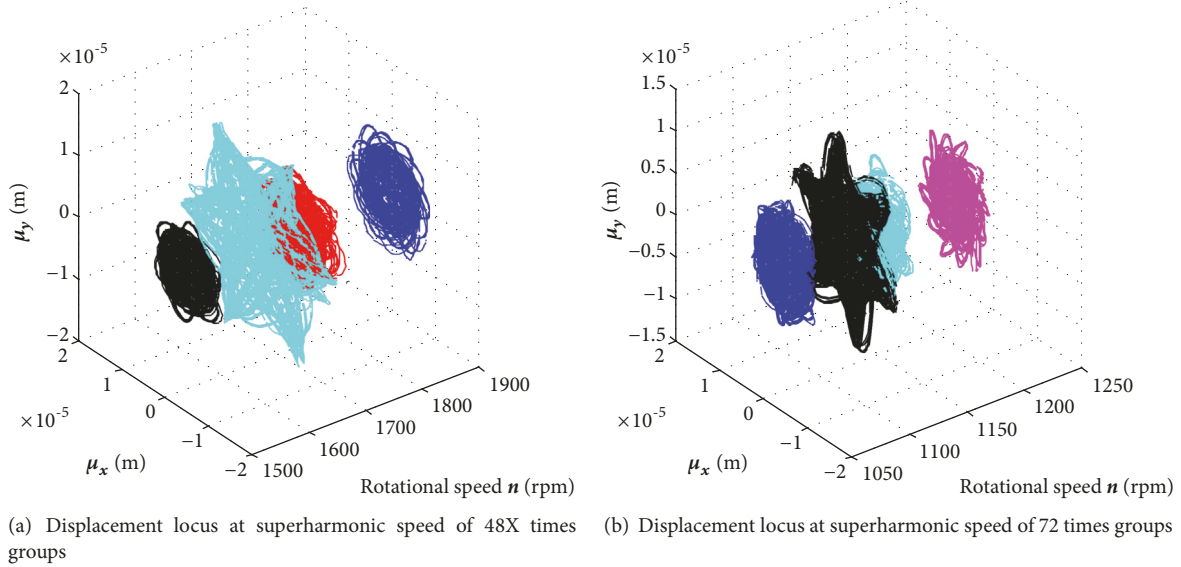


FIGURE 18: Displacement locus at superharmonic speed of other groups.

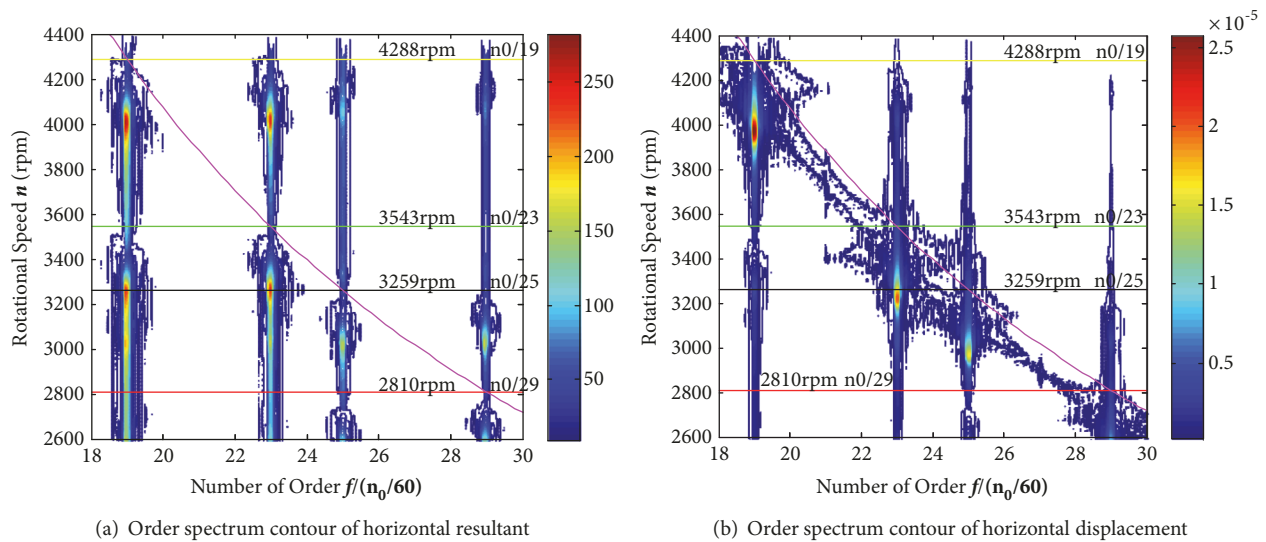


FIGURE 19: Order spectrum of resultant & displacement in 24X groups.

found. Through above research, the following conclusions are drawn.

The lateral vibration equation of the rotor can be established effectively with finite element method. The critical rotational speed and vibration mode of the rotor could be obtained by the modal analysis at different speeds.

The frequency distribution of the electromagnetic resultant in amplitude spectrum is related to rotational speed, current switchover frequency, and current wave, but the frequency distribution of the displacement is also closely related to the first-order critical speed of the rotor. In rated speed, the maximum vibration displacement shall not exceed the airgap length. The rotor cannot work regularly when the speed approaches the first critical speed of the rotor.

When the rotor runs at some specific speeds, i.e., some harmonic frequency component equals the first-order critical speed of rotor, superharmonic resonance of the rotor happens and the lateral displacement locus shows rich diversity. In displacement spectrum, the amplitude of the harmonic component near the critical rotational speed is maximal.

Main external force of the rotor can be characterized quickly, and the lateral vibration characteristics of the rotor under the interaction between electromagnetic resultant and vibration displacement could be mastered timely through this work, which will be very helpful for the design and vibration evaluation of SRM.

In summary, we have studied the vibration characteristics and superharmonic resonance of the eccentric rotor in SRM by the methods of analytical modeling and numerical

simulation. The results have important reference value for evaluating the vibration characteristics of the rotor. On the premise that only the initial SRM structure, silicon steel, and material parameters are available, we can quickly obtain the vibration displacement locus and frequency distribution rule at some typical rotational speed through this method. All of these can be helpful for the early vibration evaluation, such as obtaining the critical rotational speed of the rotor and optimizing the rotor structure parameters aimed at vibration reduction.

Data Availability

The data used to support the findings of this study are included within the article.

Conflicts of Interest

The authors declare that they have no conflicts of interest.

Acknowledgments

This work presented in this paper is supported by the National Natural Science Foundation of China (Grants nos. 11372211 and 11672349) and the National 973 Project of China (Grant no. 2014CB046805).

References

- [1] C. Gan, J. Wu, S. Yang, and Y. Hu, "Phase Current Reconstruction of Switched Reluctance Motors from DC-Link Current Under Double High-Frequency Pulses Injection," *IEEE Transactions on Industrial Electronics*, vol. 62, no. 5, pp. 3265–3276, 2015.
- [2] P. Di Barba, M. E. Mognaschi, S. Wiak, M. Przybylski, and B. Slusarek, "Optimization and measurements of switched reluctance motors exploiting soft magnetic composite," *International Journal of Applied Electromagnetics & Mechanics*, vol. 57, no. 6, pp. 1–11, 2018.
- [3] W. Hua, H. Hua, N. Dai, G. Zhao, and M. Cheng, "Comparative Study of Switched Reluctance Machines with Half-and Full-Teeth-Wound Windings," *IEEE Transactions on Industrial Electronics*, vol. 63, no. 3, pp. 1414–1424, 2016.
- [4] H.-Y. Yang, Y.-C. Lim, and H.-C. Kim, "Acoustic noise/vibration reduction of a single-phase SRM using skewed stator and rotor," *IEEE Transactions on Industrial Electronics*, vol. 60, no. 10, pp. 4292–4300, 2013.
- [5] C. Lin and B. Fahimi, "Prediction of radial vibration in switched reluctance machines," *IEEE Transactions on Energy Conversion*, vol. 28, no. 4, pp. 1072–1081, 2013.
- [6] X. Guo, R. Zhong, M. Zhang, D. Ding, and W. Sun, "Fast Computation of Radial Vibration in Switched Reluctance Motors," *IEEE Transactions on Industrial Electronics*, vol. 65, no. 6, pp. 4588–4598, 2018.
- [7] A. H. Isfahani and B. Fahimi, "Comparison of mechanical vibration between a double-stator switched reluctance machine and a conventional switched reluctance machine," *IEEE Transactions on Magnetics*, vol. 50, no. 2, pp. 293–296, 2014.
- [8] C. Liu, X. Y. Zhu, and X. W. Qing, "Modeling and analysis of switched reluctance machine considering rotor dynamics," *Proceedings of the Csee*, vol. 28, no. 3, pp. 83–89, 2008.
- [9] I. Husain, A. Radun, and J. Nairus, "Unbalanced force calculation in switched-reluctance machines," *IEEE Transactions on Magnetics*, vol. 36, pp. 330–338, 2000.
- [10] M. N. Anwar and I. Husain, "Radial force calculation and acoustic noise prediction in switched reluctance machines," *IEEE Transactions on Industry Applications*, vol. 36, no. 6, pp. 1589–1597, 2000.
- [11] Y. Yang, Z. Deng, X. Cao, G. Yang, and X. Wang, "Magnetic radial force model of bearingless switched reluctance motors," *Electric Machines & Control*, vol. 03, no. 2009, pp. 377–382, 2009.
- [12] J. J. Zhang, R. Long, H. J. Zhang, and X. Q. Ma, "Analytical and FEM Modeling of Electromagnetic Radial Force for Switched Reluctance Motor," *Applied Mechanics and Materials*, vol. 121–126, pp. 3765–3769, 2011.
- [13] X. Wang, B. Ge, J. Wang, and F. J. T. E. Ferreira, "Radial force analytic modeling for a novel bearingless switched reluctance motor when considering rotor eccentricity," *Electric Power Components and Systems*, vol. 42, no. 6, pp. 544–553, 2014.
- [14] C. P. Weiss, A. Hofmann, F. Qi, and R. W. De Doncker, "Analysis and modelling of rotor eccentricity for switched reluctance machines," in *Proceedings of the 1st International Conference on Power Electronics, Machines and Drives, (IET '14)*, pp. 1–6, 2014.
- [15] C. Grabner and E. Schmidt, "Novel comparisons of nonlinear magnetic surface and volume forces inside 6/4 and 24/16 switched reluctance motor drives," in *Proceedings of the IEEE International Electric Machines and Drives Conference, IEMDC 2003*, pp. 229–234, June 2003.
- [16] D.-H. Lee, S.-Y. Ahn, and J.-W. Ahn, "A simple negative torque compensation scheme for a high speed switched reluctance motor," *Journal of Power Electronics*, vol. 12, no. 1, pp. 58–66, 2012.
- [17] S. I. Nabeta, I. E. Chabu, L. Lebensztajn, D. A. P. Corrêa, W. M. Da Silva, and K. Hameyer, "Mitigation of the torque ripple of a switched reluctance motor through a multiobjective optimization," *IEEE Transactions on Magnetics*, vol. 44, no. 6, pp. 1018–1021, 2008.
- [18] H. Zhang, W. Xu, S. Wang, Y. Huangfu, G. Wang, and J. Zhu, "Optimum Design of Rotor for High-Speed Switched Reluctance Motor Using Level Set Method," *IEEE Transactions on Magnetics*, vol. 50, no. 2, pp. 765–768, 2014.
- [19] K. H. Ha and J. P. Hong, "Dynamic rotor eccentricity analysis by coupling electromagnetic and structural time stepping FEM," *IEEE Transactions on Magnetics*, vol. 37, no. 5 I, pp. 3452–3455, 2001.
- [20] K.-H. Ha, J.-P. Hong, G.-T. Kim, K.-C. Chang, and J. Lee, "Orbital analysis of rotor due to electromagnetic force for Switched Reluctance Motor," *IEEE Transactions on Magnetics*, vol. 36, no. 4 I, pp. 1407–1411, 2000.
- [21] K. N. Srinivas and R. Arumugam, "Static and dynamic vibration analyses of switched reluctance motors including bearings, housing, rotor dynamics, and applied loads," *IEEE Transactions on Magnetics*, vol. 40, no. 4 I, pp. 1911–1919, 2004.
- [22] A. Saxena, M. Chouksey, and A. Parey, "Effect of mesh stiffness of healthy and cracked gear tooth on modal and frequency response characteristics of geared rotor system," *Mechanism and Machine Theory*, vol. 107, pp. 261–273, 2017.
- [23] Y. Xu, J. Zhou, L. Di, C. Zhao, and Q. Guo, "Active magnetic bearing rotor model updating using resonance and MAC error," *Shock and Vibration*, vol. 2015, Article ID 263062, 9 pages, 2015.

- [24] H. Banggui and Y. Zhaoli, "The study of the influence of rolling bearing parameters on the dynamic characteristics of the main shaft," *Journal of Kunming University of Technology: Polytechnic Edition*, vol. 24, no. 3, pp. 59–63, 1999.
- [25] T. Ito and K. Akatsu, "Electromagnetic Force Acquisition Distributed in Electric Motor to Reduce Vibration," *IEEE Transactions on Industry Applications*, vol. 53, no. 2, pp. 1001–1008, 2017.
- [26] C. R. Morrison, M. W. Siebert, and E. J. Ho, "Electromagnetic forces in a hybrid magnetic-bearing switched-reluctance motor," *IEEE Transactions on Magnetics*, vol. 44, no. 12, pp. 4626–4638, 2008.
- [27] Y. W. Kwon and H. Bang, *The Finite Element Method using MATLAB*, CRC Press, 2000.
- [28] W. Xucheng, *Finite Element Method*, Tsinghua University Press, Beijing, China, 2003.

